Annu. Rev. Nucl. Part. Sci. 2004. 54:141–74
doi: 10.1146/annurev.nucl.53.041002.110618

THE BROOKHAVEN MUON ANOMALOUS MAGNETIC MOMENT EXPERIMENT

David W. Hertzog[1] and William M. Morse[2]
[1]*Department of Physics, University of Illinois at Urbana-Champaign, Urbana, Illinois 61801; email: hertzog@uiuc.edu*
[2]*Physics Department, Brookhaven National Laboratory, Upton, New York 11973-5000; email: morse@bnl.gov*

Key Words $(g-2)$, standard model, precision measurement, storage ring, precession frequency

PACS Codes 13.40.Em, 12.15.Lk, 14.60.Ef

■ **Abstract** The E821 Experiment at the Brookhaven Alternating Gradient Synchrotron has measured the muon anomalous magnetic moment a_μ to a relative precision of 0.5 parts per million. This effort required a new beamline, a super-ferric muon storage ring with a highly uniform magnetic field, a precision magnetic field measurement system, and electromagnetic calorimeters to record the electrons from muon decay, which carry the essential spin precession frequency information. Data obtained over five years resulted in more than nine billion analyzed events, in nearly equal samples of both muon charges. The experimental results $a_{\mu^+} = 11659203(8) \times 10^{-10}$ and $a_{\mu^-} = 11659214(9) \times 10^{-10}$ are consistent with each other, as predicted by the *CPT* invariance theorem. The combined result $a_{\mu^\pm} = 11659208(6) \times 10^{-10}$ is 0.9–2.4 standard deviations higher than predicted by theory; the range depends on the method employed to obtain the hadronic vacuum polarization term in the standard-model calculation. We review the experimental design, physical realization, and analysis procedures and compare the results to the theoretical prediction.

CONTENTS

1. INTRODUCTION

It was discovered early in the twentieth century that atoms are composed of protons, neutrons, and electrons, which have an intrinsic angular momentum of $\hbar/2$. A new quantum number of spin (S) was assigned; these particles have $S = 1/2$. However, spin is not just an additional quantum number. It fundamentally affects the symmetry properties of elementary particles. For example, the spin wavefunction rotation operator in quantum mechanics (1) is $e^{iS\theta}$. Thus, a rotation of the spin-1/2 wave function through 360° gives the wave function with a minus sign! It is exactly this property that distinguishes the particles that make up everyday matter with Fermi-Dirac statistics from those that transmit forces, such as the photon, which has $S = 1$ and Bose-Einstein statistics (1).

Charged particles with angular momentum produce a magnetic field, which is characterized by their magnetic moment. Classically, the magnetic moment is the current due to the rotating charge times the enclosed area: $\mu = IA$. Classically and in quantum theory, the interaction energy with an external magnetic field $\vec{B}$ is $\vec{\mu} \cdot \vec{B}$. The magnetic moment associated with orbital angular momentum L of an electron in an atom is

$$\vec{\mu_L} = \frac{e\vec{L}}{2m_e c}, \qquad 1.$$

where m_e is electron mass and c is the speed of light in vacuum. The magnetic moment of the electron associated with its spin angular momentum is

$$\vec{\mu_s} = \frac{ge\vec{S}}{2m_e c}. \qquad 2.$$

Because the spin quantum number does not have a classical analogue, g was put in as an arbitrary factor to account for the unknown physics. The Dirac equation in 1928 predicted $g = 2$ for a spin-1/2 particle without substructure (2). Measurements of the g value of the electron were consistent with 2. However, the proton g value was measured to be $g_p = 5.8$, and perhaps more surprising, the g value of the neutron was measured to be $g_n = -3.8$, in units of the proton e/m. This is a surprising result because the neutron has no net charge and therefore its magnetic moment is entirely "anomalous." Large baryon magnetic moments turned out to be a harbinger for new physics and were finally explained in the 1960s by the constituent quark model (3), which predicted $g_p/g_n \simeq -3/2$, in quite good agreement with the measured $g_p/g_n = -1.459$. Attempts in the 1930s to calculate the first-order correction to $g = 2$ for a structureless particle gave infinity (4).

In the late 1940s, a more precise measurement of the electron g value was made: $g_e = 2.002\ (5)$. The anomalous magnetic moment is defined as

$$a = \frac{g-2}{2}. \qquad 3.$$

Soon after the announcement of the experimental value, Schwinger (4) was able to calculate the first-order correction to $g = 2$ for a pointlike spin-1/2 particle: $a = \alpha/2\pi$, where $\alpha = e^2/\hbar c = 7.3 \times 10^{-3}$. Once again, measurements of the anomalous magnetic moment revealed new physics; this time it was quantum electrodynamics (QED). Now the race was on between the theorists and the experimentalists to test the contemporary "standard model of elementary particles" with precision measurements of lepton anomalous magnetic moments compared to the calculations. The race continues even to this day. A companion article in this volume discusses the theoretical calculation of the anomalous magnetic moment of the muon.

The "mu meson" was discovered in cosmic rays in the 1930s. Its existence was thought to explain the interaction between a proton and a neutron: A proton could morph into a neutron by exchange of a virtual spin-zero meson (6). However, it was discovered in the 1940s that the "mu meson" did not interact strongly with neutrons and protons, and that it was a spin-1/2 particle, not a meson; in fact, it seems to be simply a heavy copy of the electron. When I.I. Rabi was told of these astounding developments, he asked, "Who ordered that?" The muon mass is 206.8 times the electron mass. The mass of the "pi meson," or pion, is 1.32 times the muon mass. In the 1970s, yet another lepton was discovered: the τ mass is 16.8 times the muon mass (7).

In the 1970s, the weak interaction was unified with QED (8). Figure 1 shows the dominant charged- and neutral-current electroweak Feynman diagrams that contribute to the anomaly. Their contribution to the electron anomaly relative to $\alpha/2\pi$ is 0.04 parts per billion. This is much smaller than the experimental uncertainty in α. However, the contribution to the muon anomaly relative to $\alpha/2\pi$ is 1.7 parts per million (ppm). This is because the sensitivity to a mass scale Λ much greater than the mass of the lepton m_l behaves generally as

$$\delta a_l \propto \frac{m_l^2}{\Lambda^2}. \qquad 4.$$

Thus, precision measurements of the anomalous magnetic moment of the muon are $\approx(200)^2$ times more sensitive to new physics at large mass scales than comparable precision measurements made with electrons (9).

However, just as the Dirac theory had inconsistencies (infinities) before QED, the standard model has inconsistencies above the electroweak mass scale. One solution to these inconsistencies is to postulate a new symmetry between fermions and bosons, called supersymmetry (see, e.g., (10)). It was pointed out in the early 1990s that the supersymmetric contribution to a_μ could be larger than the electroweak contribution (11).

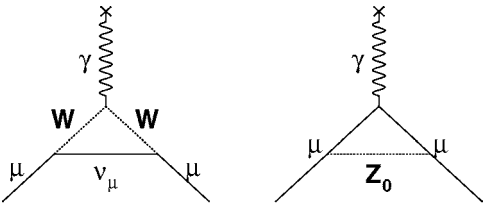

(a) Charged current (b) Neutral current

Figure 1 Feynman diagrams for the lowest-order electroweak corrections to a_μ.

Because the muon has larger mass than the electron, it decays to an electron and two neutrinos by the weak interaction, with $c\tau = 660$ m, where τ is the muon lifetime. The decay violates parity (12); the expectation value of $\vec{S}_\mu \cdot \vec{P}_e$, where S_μ is the spin of the muon and P_e is the momentum of the electron,[1] is nonzero, so the electron direction is correlated to the muon spin direction. This provides a beautiful way to measure the muon spin direction at the time of the decay. Parity violation in weak decays was a tremendous surprise when it was discovered in the late 1950s; the spin of the leptons (antileptons) produced is anti-aligned (aligned) with their momentum as $\beta = v/c \to 1$, where v is the velocity in the decay rest frame. It is parity violation that makes a sensitive measurement of the anomalous magnetic moment of the muon possible, first as a muon spin polarizer—in $\pi \to \mu\nu$ decay—and then as a muon spin analyzer.

The lepton lifetime is proportional to the inverse fifth power of the mass, so the τ lepton is much too heavy for this type of experiment: $c\tau$ is only 9×10^{-5} m. It turns out that the muon mass gives an almost perfect compromise between long lifetime, which benefits the experimentalist, and large mass, which benefits the theorist.

1.1. Vernon W. Hughes and the Muon

Vernon W. Hughes, who was Rabi's student, organized a workshop at Brookhaven National Laboratory in 1984 with the aim of studying the possibility of measuring the anomalous magnetic moment of the muon with a precision better than the electroweak contribution. The motivation was to search for new-physics contributions to the anomaly at mass scales in excess of the electroweak mass scale of 10^{11} eV. Hughes already had extensive experience (13) with precision measurements of muonium, the bound state of a muon and an electron. Six members of the teams that had carried out a series of beautiful experiments at CERN (14–16), which measured the muon anomaly in the late 1950s through the mid 1970s, attended

[1]E821 used both μ^+ and μ^- beams, which detected positrons and electrons, respectively. We use the language for μ^- and "decay electrons" throughout this article for simplicity.

Figure 2 Photograph from 1984 workshop at Brookhaven National Laboratory. Standing, from left: G. Danby, J. Field, F. Farley, E. Picasso, and F. Krienen; kneeling, from left: J. Bailey, V. Hughes, and F. Combley.

the workshop (Figure 2): J. Bailey, F. Combley, J. Field, E. Picasso, F. Farley, and F. Krienen. The latter two went on to collaborate extensively on the Brookhaven experiment, E821.

2. THE PRINCIPLE OF THE MEASUREMENT

The measurement of the anomalous magnetic moment of the muon requires a polarized muon beam that interacts with an external magnetic field, after which the mean muon spin direction is determined. High-energy proton-nucleus collisions are used to create intense pion beams by the strong interaction. The pion weak decay ($\pi \rightarrow \mu\nu$) creates a source of secondary muons. Because the weak decay violates parity, a muon beam with high polarization can be obtained. The first CERN experiment (14) used a low-energy muon beam, which passed through a long magnet and onto a stopping target where the spin direction was measured. However, most of the muons were lost; this experiment collected less than one muon decay per second. The second experiment (15) used a muon storage ring. The protons were brought onto a target inside the ring, and a few muon decays were collected per fill. The third experiment (16) improved by injecting a pion beam into the storage ring. About 100 muons were stored per fill. The relative

accuracy of the final CERN experiment was $\delta a_\mu/a_\mu = 10$ ppm for both the μ^- and its antiparticle the μ^+. It became clear to many at the 1984 workshop that a muon beam injected into a storage ring could produce $\sim 10^4$ muons stored per fill at Brookhaven, yielding a precision an order of magnitude better than that of the CERN experiments.

The experimental observable for parity violation in the weak decay $\mu \to e\nu\overline{\nu}$ is $\vec{S}_\mu \cdot \vec{P}_e$. In a muon storage ring with relativistic $\gamma = E_\mu/m_\mu c^2$, the decay rate is

$$\frac{dN_e(p_e)}{dt} = N_0 e^{-t/\gamma\tau}[1 + A(p_e)\cos(\theta)], \qquad 5.$$

where $\hat{S}_\mu \cdot \hat{P}_\mu = \cos(\theta)$, so we need to follow $\hat{S}_\mu \cdot \hat{P}_\mu$ for a muon in a storage ring (17). A muon in a uniform magnetic field with $\vec{B} \cdot \vec{P}_\mu = 0$ has cyclotron frequency

$$\omega_c = \frac{eB}{m_\mu c\gamma} \qquad 6.$$

because of the Lorentz force: $\vec{F} = d\vec{p}/dt = e\vec{v} \times \vec{B}$. This is the rate at which the momentum rotates. The rate at which the muon spin precesses in an external magnetic field is

$$\frac{d\vec{S}}{dt} = \vec{\mu} \times \vec{B} \qquad 7.$$

because of the torque on the magnetic moment. This equation is for a muon at rest and gives the Larmor frequency $\omega_L = geB/2m_\mu c$. The muon spin precession rate in a storage ring is

$$\omega_s = \frac{eB}{m_\mu c\gamma} + \frac{ea_\mu B}{m_\mu c}; \qquad 8.$$

this equation includes the Thomas precession, which takes into account that the muon is in a rotating reference frame and not an inertial frame (17). The difference between the spin and momentum rotation rates (anomalous spin precession) is

$$\omega_a \equiv \omega_s - \omega_c = \frac{ea_\mu B}{m_\mu c}. \qquad 9.$$

A miracle has occurred! Equation 9 contains no γ. The constant $e/m_\mu c$ is well known from other experiments (13). So, by accurately measuring ω_a in an accurately determined magnetic field, it is possible to obtain a_μ. In E821, the muon storage ring has a very uniform magnetic field with electrostatic quadrupole focusing. The anomalous spin precession for magnetic and electric fields when $\vec{B} \cdot \vec{P} = \vec{E} \cdot \vec{P} = 0$ is

$$\vec{\omega}_a = \frac{e}{m_\mu c}\left[a_\mu \vec{B} - \left(a_\mu - \frac{1}{\gamma^2 - 1}\right)(\vec{\beta} \times \vec{E})\right]. \qquad 10.$$

For the momentum of the muon beam, we chose the so-called magic momentum

$$p_\mu = \frac{m_\mu c}{\sqrt{a_\mu}} = 3.09\,\mathrm{GeV/c}, \qquad 11.$$

where the coefficient in front of the electric field term is close to zero. The magic momentum can be understood qualitatively as follows. As $\beta \to 1$, the effect of an electric field is the same as the effect of a magnetic field, and thus the precession rate of the magnetic moment is greater than the rate of rotation of the momentum by the anomaly. However, as $\gamma \to 1$, the electric field has a much larger effect on the momentum rotation rate compared to the precession rate of the magnetic moment. The magic momentum is where the electric field has the same effect on both the magnetic moment precession rate and the momentum rotation rate. In a real storage ring, where $\vec{B} \cdot \vec{P}$ is not zero and not all muons are at the magic momentum, corrections must be applied, which we discuss later.

2.1. Blind Data Analysis Philosophy

The determination of a_μ depends on the ratio between the precise and independent measurements of ω_a and B. In practice, the magnetic field is measured in units of the free proton precession frequency ω_p. The muon anomaly a_μ is obtained by the following sequence of equalities:

$$\begin{aligned} a_\mu &= \frac{a_\mu}{\frac{g}{2} - \frac{g-2}{2}} = \frac{\left(\frac{e}{m_\mu c} a_\mu B\right)}{\left(\frac{e}{m_\mu c}\frac{g}{2} B - \frac{e}{m_\mu c} a_\mu B\right)} \\ &= \frac{\omega_a}{\omega_L - \omega_a} = \frac{\omega_a/\omega_p}{\omega_L/\omega_p - \omega_a/\omega_p} = \frac{R}{\lambda - R}, \end{aligned} \qquad 12.$$

where the ratio $R = \omega_a/\omega_p$ is determined in our experiment and the muon-to-proton magnetic moment ratio λ is obtained from muonium hyperfine-level structure measurements (18). The most recent measurement of λ, led by Hughes, is 3.18334539(10).

The E821 Experiment had five running periods, described below. For each of the high-statistics efforts, multiple independent analyses of both the magnetic field and the precession frequency were made by different groups within the Collaboration. Two largely independent analyses of the precision magnetic field data were performed for each data set. Their results for ω_p agreed to better than 0.05 ppm each time. The precession analysis involved a more elaborate effort, beginning with separate productions of the raw data into electron energies and times-of-arrival at the detectors. From each of two processed data sets, at least two independent analysis strategies emerged per running period. The concept was to explore the many ways ω_a could be extracted from the data, to make sure the result did not depend on the approach, and to cross check to avoid mistakes. During each analysis period of a year plus, the ω_p and ω_a analysis teams each reported their preliminary results to the Collaboration with secret frequency offsets. This meant that no individual

ever knew enough information to compute a_μ from Equation 12. Only after the analyses were complete and the Collaboration voted to accept the results as final were the offsets removed and the calculation of a_μ made.

2.2. Running Periods and Data Collected

E821 began taking data in 1997, before the installation of the muon kicker. In ~160 h of "pion injection" data, a_μ was measured with a precision of 13 ppm (19), using a technique that closely matched that of the CERN-III effort (16). This measurement established E821 as a working experiment, but only in 1998, when the muon kicker was commissioned, did it become evident that our new approach could offer a significant improvement over CERN's. The immediate effect of direct injection of muons was quite dramatic. The initial pion-induced flash—an enormous burst of background particles occurring when pions from the injection crashed into the detectors and magnet walls—was reduced by a factor of 60, and the useful muon decays per fill increased by a factor of 10. With only two weeks of data taking, a_μ was measured to a precision of 5 ppm (20). The 1998 run was terminated abruptly because of an upstream beamline element failure, but the 1999 run continued a few months later with no important changes in the system of muon storage equipment or detectors. Several months of data accumulation led to the first important result (21), with a precision of 1.3 ppm. It disagreed with the concomitant standard-model calculation by 2.6 standard deviations, sparking a lively physics conversation with both conventional and exotic explanations for the deviation. The 1999 precession data also revealed unanticipated experimental subtleties principally due to the dependence of the detector acceptance on the muon beam betatron motion—the coherent betatron oscillation (CBO) effect—as described in detail in Section 5.3. The CBO effect is fully understood, but it was responsible for the largest systematic uncertainty on the high-statistics data taken during 2000. In 2001, the beam polarity was reversed for a three-month μ^- run. The CBO systematic error was reduced significantly by using different betatron frequencies for the storage ring. The analysis was completed (23) in late 2003. Table 1 summarizes the data periods, statistics and results.

3. BEAMLINE AND STORAGE RING

A precision measurement of the anomalous magnetic moment requires an intense source of polarized muons injected into a storage ring with a highly uniform magnetic field. A secondary beamline channel, which transports pions (and their decay muons) following high-energy proton-nucleus collisions, must be well-matched to the storage ring acceptance. A fast kicker must fire at the time of injection to place the muons on allowed orbits inside the ring. Electrostatic quadrupoles provide focusing to maintain a stored muon beam in the ring. Finally, a network of fixed and movable nuclear magnetic resonance (NMR) probes is needed to monitor and measure the magnetic field.

TABLE 1 Summary of a_μ results from BNL Experiment E821

Year	Injected Particle	Events [10^9]	$a_\mu \times 10^{10}$	Precision [ppm]	Reference
1997	π^+	0.01	11659251(150)	13	(19)
1998	μ^+	0.08	11659191(59)	5	(20)
1999	μ^+	0.95	11659202(15)	1.3	(21)
2000	μ^+	4.0	11659204(9)	0.7	(22)
2001	μ^-	4.0	11659214(9)	0.7	(23)
Average	—	~9.0	11659208(6)	0.5	

The intense proton beam from the Brookhaven Alternating Gradient Synchrotron (AGS) strikes a nickel target to create a source of energetic charged pions. The beamline collects pions with momentum slightly above the magic momentum. The beamline length of 122 m is well matched to the pion decay length, $\beta\gamma c\tau = 174$ m. Muons with close to the magic momentum, which match the emittance of the storage ring injection system, are transported to the inflector magnet (24). The emittance ϵ of a beam of particles is the area enclosed in an x versus $\dot{x}$ or y versus $\dot{y}$ scatter plot, where $\dot{x} = \frac{dx}{ds}$, $\dot{y} = \frac{dy}{ds}$, and s is the path length. It is well known in optics that a light beam with finite spot size but very small divergence can be focused by a lens to a very small spot size with finite divergence. The emittance of the beam is conserved with perfect lenses. The same emittance formulism is used for the design of particle beams. Table 2 lists the AGS parameters used for E821, and Table 3 gives the beamline parameters.

The inflector magnet cancels the storage ring magnetic field, so the incoming beam is close to the storage ring acceptance on a parallel trajectory as it enters the storage ring field. Figure 3 represents the end of the inflector magnet in the muon storage ring.

The design requirements for the muon storage ring are a very uniform magnetic field at the magic momentum with a large muon storage region to maximize the

TABLE 2 Proton beam parameters of the Alternating Gradient Synchrotron

Parameter	Value
N_p per cycle	5×10^{13}
Repetition rate	0.4 Hz
Proton momentum	24 GeV/c
Number of bunches	12
Bunch width (σ)	25 ns
Bunch extraction rate	30 Hz

TABLE 3 Parameters of the pion beamline

Parameter	Value
Pion beam horizontal emittance	42π mm-mrad
Pion beam vertical emittance	56π mm-mrad
Inflector magnet length	1.7 m
Inflector horizontal aperture	$\pm$ 9 mm
Inflector vertical aperture	$\pm$ 28 mm
Beamline pions per 24 GeV proton	10^{-5}
Muons per beamline pion	6×10^{-3}
Muon polarization	95%

number of stored muons. A super-ferric design (25) was chosen: Superconducting coils with inductance $L = 0.48$ H and resistance—from the leads—of 1 mΩ give a time constant $L/R = 4800$ s. The field is shaped by iron to ease the coil mechanical tolerances and allow local field adjustments. The magnetic field was chosen to be $B_0 = 1.45$ T, well below the iron saturation field of $\simeq$1.6 T. This gives a central orbit radius of $R_0 = 7.11$ m for muons at the magic momentum of 3.09 GeV/c. The chosen diameter of the muon storage region was 90 mm, a compromise between the requirements of high muon acceptance and a uniform magnetic field with very small higher-order multipoles. Because of the technical difficulty of the inflector magnet design (24), the inflector beam channel is smaller than the muon storage region, especially in the horizontal dimension. In terms of

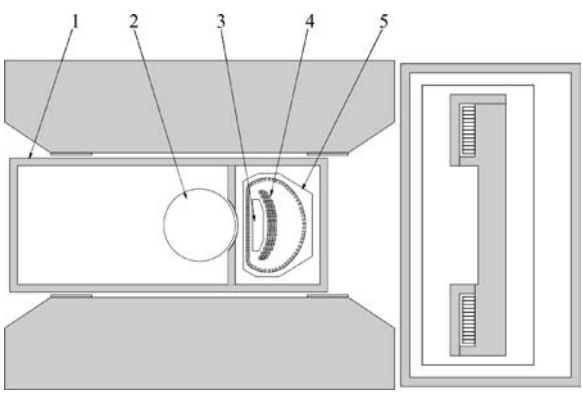

Figure 3 Schematic diagram of the downstream end of the 1.7-m-long inflector magnet showing the vacuum chamber (1), muon storage region (2), inflector beam channel (3), superconducting inflector coil (4), and inflector magnet body (5), as well as the storage ring outer coil and pole iron.

TABLE 4 Muon storage ring parameters

Parameter	Value
Design magnetic field (B_0)	1.45 T
Design current	5200 A
Outer coil windings	48
Central orbit radius (R_0)	7.11 m
Muon storage region diameter	90 mm
Magnet gap	18 cm
Stored energy	6 MJ
Muon cyclotron frequency	6.7 MHz
Muon $g-2$ frequency	229 kHz

emittance, the x dimension of the muon storage region is not filled, whereas the $\dot{x}$ dimension is filled. Figure 4 shows a photograph of the completed storage ring magnet in 1997. The storage ring magnet parameters are given in Table 4.

Figure 5 shows a schematic drawing of the cross section of the storage ring magnet. The magnet was designed as a "kit" that would allow shimming to obtain a uniform magnetic field:

- Iron shim plates on the top and bottom of the 12 yoke sections allowed us to adjust the yoke reluctance by inserting precision spacers to create an air gap.
- One thousand iron wedge shims were placed in the air gaps between the yoke and pole steel to allow adjustments to the pole reluctance.
- Seventy-two iron edge shims were screwed onto the edges of the poles, enabling adjustments to the higher-order multipoles of the magnetic field.
- One hundred conductors were attached to the pole face surfaces to fine-tune the higher-order multipoles. These conductors were spaced every 2.5 mm on a printed circuit board, and currents were introduced at one location with twisted pair multiconductor cable. The magnetic field uniformity over the 90-mm-diameter muon storage region, integrated around the ring, was typically $\pm$ 10 ppm before the pole face windings were used, and $\pm$ 1 ppm after the pole face windings were adjusted.

Because the beam enters the main field about 77 mm outside the center of the storage region, a fast kick of about 77 mm/7.1 m = 10 mrad is needed when the beam crosses the central orbit after about one quarter of the storage ring circumference. This is technically challenging because of the requirements of a very uniform magnetic field:

- The kicker magnet must fit in the storage ring magnet gap.

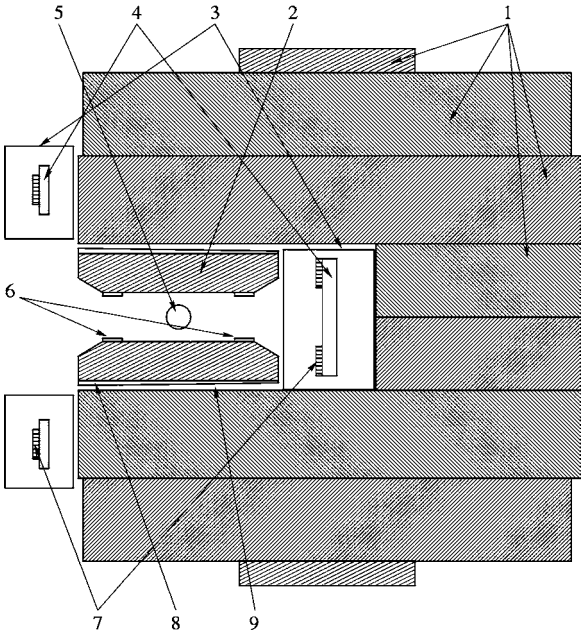

Figure 5 Schematic diagram of the cross section of the 1.45 T muon storage ring magnet showing the yoke iron (1), pole iron (2), cryostats (3), mandrels (4), muon storage region (5), edge shims (6), superconducting coils (7), wedge shims (8), and air gap (9).

- Magnetic materials are not allowed.
- Stray kicker fields should be below 0.1 ppm of the main field when muon decay data are being measured ($\approx$25 μs after injection).

The technical solution is discussed in Reference (26).

Electric quadrupoles (27) were used to focus the beam within the storage ring. Figure 6 shows a schematic of a quad section inside the vacuum chamber. The vacuum pressure was typically 5×10^{-7} Torr. The field index is proportional to the electric quadrupole gradient and is defined as

$$n = \frac{R_0}{c\beta B_0} \frac{\partial E_y}{\partial y}. \qquad 13.$$

The electric field focuses vertically but defocuses horizontally; that is, for negative muons, the top and bottom electrodes are at negative voltage whereas the side electrodes are at positive voltage. The stored muons then undergo simple harmonic motion in the vertical plane:

$$y = \sqrt{\epsilon_y \beta_y} \cos(s/\beta_y + \phi_y). \qquad 14.$$

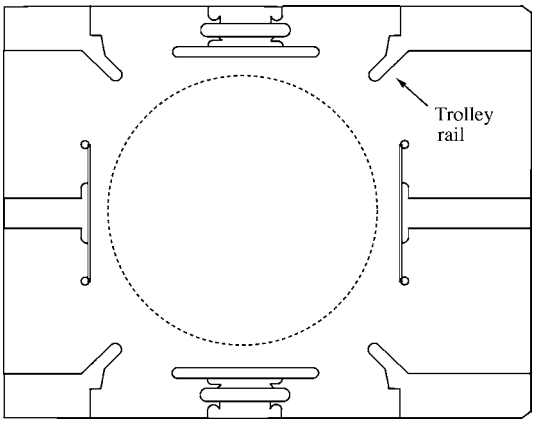

Figure 6 Schematic of electrostatic quadrupole electrodes inside the vacuum chamber. For positive muons, the top and bottom electrodes are at +24 kV; the side electrodes are at −24 kV. The NMR trolley rails can be seen between the electrodes in the $V = 0$ planes. The 9-cm-diameter storage region is depicted by the dashed circle.

For continuous quadrupole coverage, $\beta_y = R_0/\nu_y$, where the vertical tune ν_y is approximately $\sqrt{n}$. This is a good approximation for our ring, although exact calculations are used to set the high voltage. For the horizontal (actually radial $x = \rho - R_0$) plane,

$$x = x_e + \sqrt{\epsilon_x \beta_x} \cos(s/\beta_x + \phi_x), \qquad 15.$$

where x_e, the equilibrium radial position relative to the equilibrium position of a muon with magic momentum, is

$$x_e = \frac{(p - p_m)R_0}{p_m(1 - n)}. \qquad 16.$$

Here, $\beta_x \simeq R_0/\nu_x$ and the horizontal tune $\nu_x \simeq \sqrt{1 - n}$ reflects the focusing effect of the magnetic field and the defocusing effect of the electric field. As usual, one wants to avoid beam-dynamics resonances at which an integer times the horizontal tune plus an integer times the vertical tune equals an integer. Resonance lines up to fifth order with the working line $\nu_x^2 + \nu_y^2 = 1$ are shown in Figure 7, along with the tune values used during the 2000 ($n = 0.137$) and 2001 runs ($n = 0.142$ and 0.122). Short study runs taken on the resonances $n = 0.126$ and 0.148 showed increased muon losses. A fraction ($\simeq$3%) of the lost muons passed through special detectors, which provided a continuous measurement of the lost muons during the data taking.

During the first $\simeq$100 turns, asymmetric quad voltages were used to displace the beam by about 2 mm horizontally and vertically. This displacement scraped the outer edge of the beam against centered, 9-cm-diameter circular copper collimators located at several fixed positions around the ring. Without this scraping procedure,

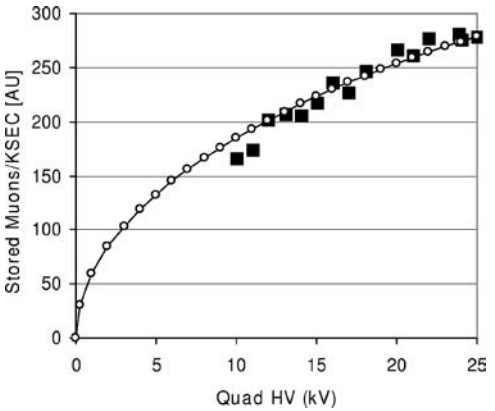

Figure 8 Measured normalized number of stored muons (*squares*) and the expected dependence (*circles*) for short runs with varying quadrupole high voltage.

the muon losses were typically $\simeq 6 \times 10^{-3}$ per muon lifetime. With scraping, the losses were $\simeq 2 \times 10^{-3}$ per muon lifetime.

An online measure proportional to the number of stored muons is plotted against electrostatic quadrupole high voltage in Figure 8. The high-voltage settings for the run in 2000 were ± 24 kV, which corresponds to $n = 0.137$. As the high voltage is increased, the vertical phase space increases, while the horizontal phase space decreases: $N_\mu \simeq \nu_x \nu_y \simeq \sqrt{n(1-n)}$, consistent with the data shown in Figure 8. High-voltage values up to ± 25 kV gave reliable operation.

An array of seven scintillating fibers 1.3 cm apart was placed directly in the muon storage region for occasional short runs to provide a snapshot of the muon flux profile ~ 1 μs after injection. Figure 9 shows the output of five central elements in the array. Fourier analysis reveals the muon cyclotron period, a small proton contamination (longer cyclotron period), and the coherent radial betatron motion. The coherent radial betatron movement is due to the beam alternately filling x and $\dot{x}$ phase space every $1/\nu_x \simeq 1.076$ turns, which is observed at one azimuthal location as $1/(1-\nu_x) \simeq 14$ turns.

Figure 10 shows muon decay calorimeter counts versus time. Fourier analysis of these data (the rapid oscillations) indicates a muon cyclotron period of 149.1 ns. Because the magnetic field is accurately known, the muon momentum distribution, or alternatively the equilibrium orbit radius with respect to the equilibrium orbit radius of a muon with the magic momentum (see Figure 11), can be obtained from the cyclotron frequency distribution. It is this very distribution that is required for a correction to ω_a for muons off the magic momentum. The slower undulation in the plot is the anomalous precession frequency ω_a. Fourier analysis also shows a peak due to the horizontal betatron motion. This is because of the variation of the detector acceptance with the muon position corresponding to $\simeq 1\%$ modulation in the counts. If the data from all detectors are added together, all Fourier analysis

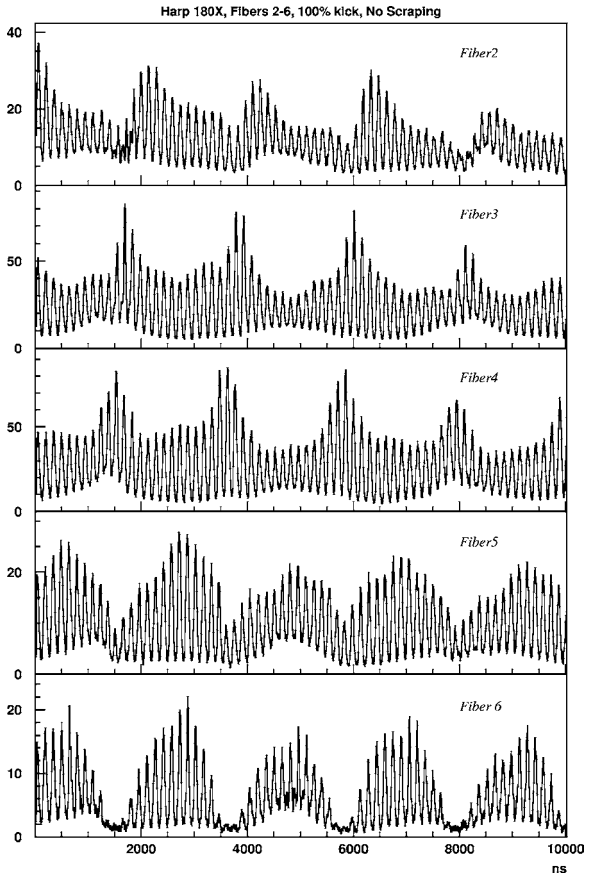

Figure 9 The output from scintillating fibers placed in the muon storage region. Fiber 4 is the central fiber; the other fibers are spaced radially by 1.3 cm. Sixty-seven turns of the muon beam can be seen. The coherent betatron oscillation is clearly visible: The beam alternates between filling the x and $\dot{x}$ phase space every $\simeq$14 turns.

peaks other than the peak at ω_a are reduced by a factor of >3 owing to the symmetry of the ring.

4. PRECISION MEASUREMENT OF THE MAGNETIC FIELD

The measurement of the magnetic field is based on pulsed proton NMR in water and makes use of a precision magnetometer developed and constructed for our experiment (28). The measured precession rate in water is then related to the free proton precession rate (29), which is accurately known: 42.577469(13) MHz/T. The internal diamagnetic shielding of the water molecule, due to the

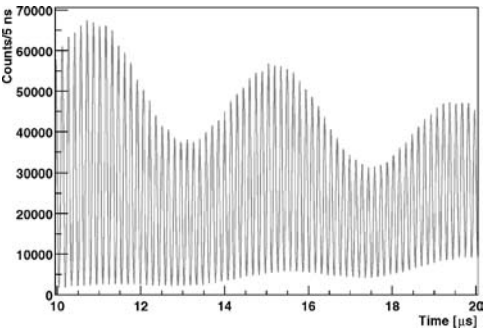

Figure 10 Time histogram from one calorimeter showing the fast rotation of the beam from 10 to 20 μs after muon injection. The rapid oscillation is the beam-bunch cyclotron frequency; the slow undulation is the $(g-2)$ frequency.

Larmor precession of the electrons in the external magnetic field, has been measured to be $\sigma = 25.790(14)$ ppm at 34.7°C. The temperature dependence is 0.01036 (30) ppm/°C. The temperature of the probe was measured to ± 1°C and the correction was made. The measurement of the magnetic field was accomplished in the following manner:

- During the muon runs, 360 "fixed" NMR probes were read out at a rate of $\simeq$2 Hz. They are embedded in machined grooves in the upper and lower plates of the aluminum vacuum chamber and consequently measure the field just outside of the actual storage volume. About 150 probes, those with the most reliable signals, are used in the offline analysis.

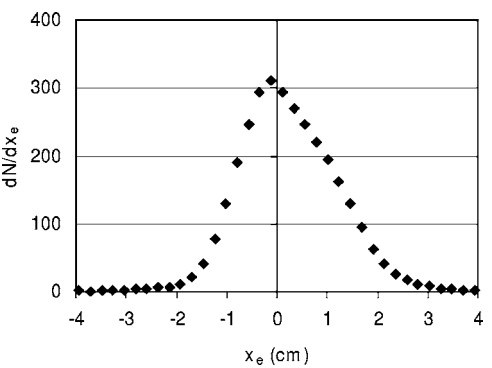

Figure 11 Fourier analysis of the time histogram from one muon decay detector gives the distribution of cyclotron frequencies for the ensemble of muons. Because the magnetic field is accurately known, this distribution can be plotted as a function of x_e, the equilibrium radius with respect to the equilibrium radius of a muon with the magic momentum.

- About twice a week during the muon runs, the beam was turned off for ∼4 h while a trolley—carrying a grid of 17 NMR probes—measured the magnetic field in the muon storage region under vacuum at ∼6000 azimuthal locations. This served to relate the fixed NMR probe readings to magnetic field values inside the muon storage region.
- During a running period, the 17 trolley probes were calibrated against a "plunging probe" in vacuum. This was accomplished by placing the plunging probe in the same spatial region as each trolley NMR probe. The trolley was positioned at the azimuthal location of the plunging probe, and the NMR frequencies were recorded. The trolley was then moved ≃1 m away and the plunging probe was inserted into the storage region at each of the locations of the trolley probes, and the NMR frequencies were recorded. This procedure was repeated several times.
- Before and after the run, the plunging probe and a subset of the trolley probes were calibrated to the "standard probe" in air. The shielding of the magnetic field due to the air molecules was measured and found to be negligible.

A correction must be made to account for the shielding of the magnetic field because of other water molecules and the glass vial. By symmetry, this correction is zero for a spherical sample. The standard NMR probe is spherical with diameter 10 mm. The bulk diamagnetic correction for the standard probe is (0 ± 0.05) ppm. The other NMR probes are cylindrical (D = 2.5 mm, L = 15 mm) because of geometrical limitations. The difference between the standard probe frequency and the trolley probe frequencies in the same magnetic field is ≃1 ppm, consistent with that expected for the effect of the bulk diamagnetism of the cylindrical probe and with the effect of the trolley materials. The uncertainty on ω_p because of the trolley probe calibration procedure was 0.09 ppm for the 2001 data. The variation of the trolley field readings with the supply voltage and with the synthesizer settings, as well as the dependence on the temperature inside the trolley shell, were measured to be small in the range of operation. The combined upper limits are included as a contribution to the systematic uncertainty. The total systematic uncertainty on ω_p was 0.17 ppm for the 2001 data (see Table 5). Figure 12 shows an azimuthally averaged field map from one of the twenty 2001 trolley runs.

5. MEASUREMENT OF ω_a

5.1. Kinematic Considerations

All measurements of the angular and energy distributions of the decay electron in the decay ($\mu^- \rightarrow e^- \bar{\nu}_e \nu_\mu$) are consistent with a $V - A$ form of the weak interaction (3). Inherent in this parity-violating form is the correlation between the decay electron trajectory and the direction of the muon spin. The angular distribution of emitted electrons from an ensemble of polarized muons at rest

TABLE 5 Systematic uncertainties for the ω_p analysis

Source of uncertainty	Size [ppm]
Absolute calibration of standard probe	0.05
Calibration of trolley probe	0.09
Trolley measurements of B_0	0.05
Interpolation with fixed probes	0.07
Uncertainty over muon distribution	0.03
Others[a]	<0.10
Total systematic error on ω_p	0.17

[a]Higher multipoles, trolley temperature and voltage response, eddy currents from the kickers, and time-varying stray fields.

is $dn/d\Omega = 1 - a(E)\cos\theta$, where $\cos\theta$ is $\hat{S}_\mu \cdot \hat{P}_e$, and we emphasize that the asymmetry, a, depends on electron energy (E). Convenient expressions for electron number n and asymmetry a can be written in terms of the fractional energy of the electron, $y = E_e/E_{e,\max}$, where $E_{e,\max}$ is very nearly equal to $m_\mu/2$, or about 52.8 MeV. These expressions are

$$n(y) = y^2(3 - 2y) \quad \text{and} \quad a(y) = (2y - 1)/(3 - 2y); \tag{17.}$$

both are plotted in Figure 13. The asymmetry is negative for low-energy electrons and rises to $a = +1$ when $y = 1$. The higher-energy electrons have the strongest

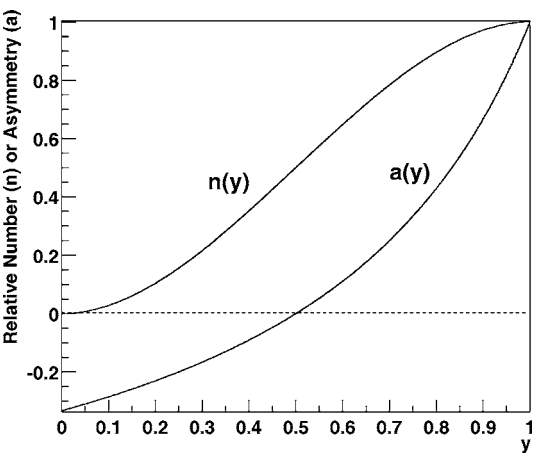

Figure 13 The electron number, n, and asymmetry, a, for muon decay at rest versus the fractional energy of the emitted electron.

correlation to the muon spin; we will be interested in these electrons in particular. But first, we must consider what happens in the laboratory frame.

The decay electron energies are related to the center-of-mass (c.m.) energy by

$$E_{e,\text{lab}} = \gamma(E_e^* + \beta P_e^* \cos\theta^*), \tag{18.}$$

where $\cos\theta^* = \hat{P}_\mu \cdot \hat{P}_e^*$. The starred quantities indicate c.m. and $\gamma = 29.3$, for our experiment at the magic momentum of 3.09 GeV/c. The lab electron energies range up to 3.1 GeV. Because the velocity of the electron in the muon rest frame is always close to c, Equation 18 can be simplified to

$$E_{e,\text{lab}} \approx \gamma E_e^*(1 + \cos\theta^*). \tag{19.}$$

This captures the important relationship for the $g - 2$ experiment, namely that the electron *energy* in the lab frame is correlated to the emitted *angle* in the c.m. frame. A high-energy electron is most likely to be detected when the muon spin is pointing opposite to the direction of muon momentum and least likely when the spin is aligned with the muon momentum. Information on the time evolution of the average spin direction of an ensemble of polarized muons in the storage ring is contained in the data of electron rate versus time. The rate of detected electrons above energy threshold E_{th} is

$$\frac{dN(t; E_{\text{th}})}{dt} = N_0 e^{-t/\gamma\tau_\mu}\,[1 + A\cos(\omega_a t + \phi)]. \tag{20.}$$

Here the normalization, N_0, asymmetry, A, and initial phase, ϕ, are all dependent on the threshold energy. The time-dilated muon lifetime is $\gamma\tau_\mu \approx 64.4\,\mu$s, and, for an energy threshold of $E_{\text{th}} = 1.9$ GeV, $A \approx 0.4$. Figure 14 shows the time spectrum of detected electrons from a portion of the data. This is the type of distribution from which the anomalous precession frequency is extracted.

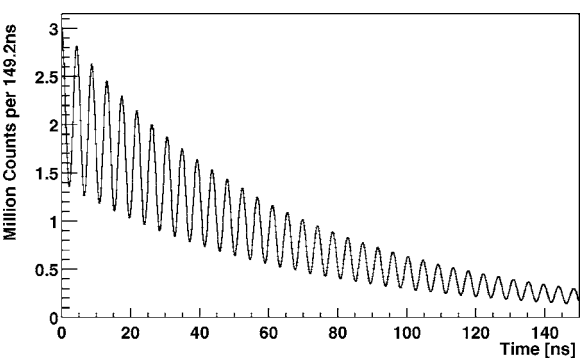

Figure 14 A snapshot of a fraction of the electron decay data. The exponential decay is multiplied by $1 + A\cos(\omega_a t + \phi)$.

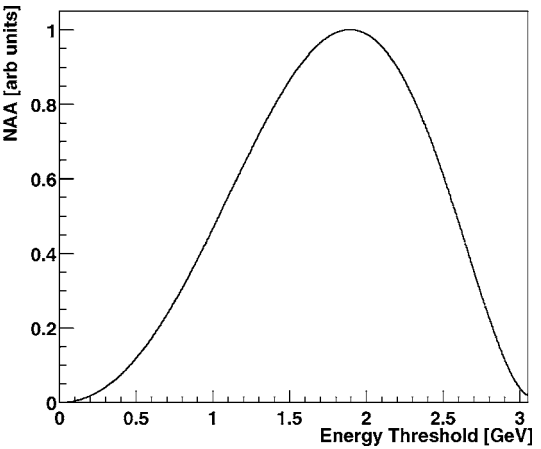

Figure 15 The figure of merit, NA^2, in the laboratory frame. The peak near 1.9 GeV indicates the importance of the highest-energy electrons in the minimization of the uncertainty on a_μ.

The uncertainty on ω_a from Equation 20 is given by

$$\delta\omega_a = \frac{1}{\gamma\tau_\mu}\sqrt{\frac{2}{NA^2}}, \qquad 21.$$

where N is the integrated number of decay electrons in the analysis. The quantity NA^2 is a figure of merit; maximizing it minimizes the statistical uncertainty on ω_a and thus a_μ. Figure 15 is a plot of NA^2 versus energy threshold. At $E_{\text{th}} \approx 1.9$ GeV, NA^2 is at a maximum, assuming equal acceptance for electrons of any energy. In practice, the threshold is set close to this optimal point for our conventional method of extracting ω_a.

5.2. Electron Detector System

Almost all of the decay electrons have momenta below 3.094 GeV/c; therefore, they curl to the inside of the ring and escape through the opening in the C-shaped magnet. Electromagnetic calorimeters intercept the electrons and provide a measure of energy and time of detection. The calorimeters are adjacent to the storage ring vacuum chambers at 15° intervals around the ring (see Figure 16). The suite of 24 detectors has an overall acceptance of about 70% for decay electrons above 1.9 GeV. Five-finger scintillator hodoscopes are positioned in front of the calorimeters; we used them to measure the vertical distribution at the detector location and, by requiring a coincidence of three adjacent hodoscopes, to monitor muons lost from the storage ring.

The design of the calorimeters was constrained by the unusual experimental demands. A gain shift ΔG in combination with a fixed threshold has the effect of changing the observed asymmetry A and phase ϕ versus time; this, in turn,

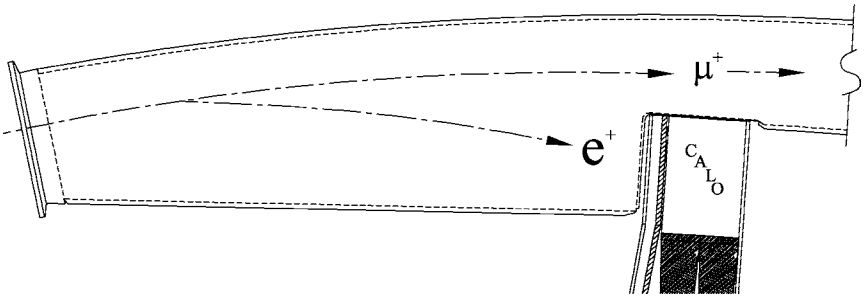

Figure 16 Top view of the scalloped vacuum chamber and the location of the calorimeter. A decay positron curls to the inside of the ring and exits the vacuum chamber nearly orthogonal to the wall.

changes the extracted value of ω_a. A time shift ΔT directly changes the fitted frequency. The stability conditions that ensure a shift of less than 0.1 ppm to ω_a are $\Delta G < 0.2\%$ and $\Delta T < 20$ ps over 200 μs. The instantaneous event rate of a few megahertz drops by almost five orders of magnitude during the 600 μs measuring period; thus, any rate-dependent detector or readout response changes must be accurately known. Further complicating the design, the voltage dividers of the photomultiplier tubes must be gated off during injection and switched back on after injection because of the very large number of lost particles at injection.

Two low-energy electrons, arriving close together in time, can be interpreted as one equivalent high-energy electron, a type of "pileup" event. Because the low-energy electrons have a shorter path to the detector than do higher-energy electrons, there is a natural phase difference versus energy inherent in the data. Unaccounted for, the ratio of fake to real high-energy electrons changes with time, having a time dependence of $\sim e^{-2t/\gamma\tau}$; that is, their rate falls twice as fast as the muon population decays. To minimize pileup, the calorimeter response and the readout system must be fast (a few nanoseconds) to enable the distinction between pulses that nearly coincide. This information should also provide a mechanism to correct the data, on average, by removing the pileup events.

The calorimeter energy resolution must be moderately good near 1.9 GeV to provide adequate energy discrimination. However, the calorimeter also must be compact to avoid a preponderance of electrons striking the side face. Usually higher density implies lower resolution.

We achieved these goals by using a compact lead-scintillating fiber calorimeter (see Figure 17) with a fractional energy resolution of $\approx 7\%$ at $E_e = 1.9$ GeV (30). Its 13 X_0 depth of 15 cm (X_0 = radiation length) is adequate to contain electromagnetic showers up to 3 GeV. The good resolution is preserved because the scallop shape in the storage ring vacuum chamber is effective in reducing the preshowering of electrons as they exit the chamber (see Figure 16).

Each calorimeter is viewed by four photomultiplier tubes, whose summed signal is recorded by a 400 MHz waveform digitizer. When the roughly 1 GeV hardware

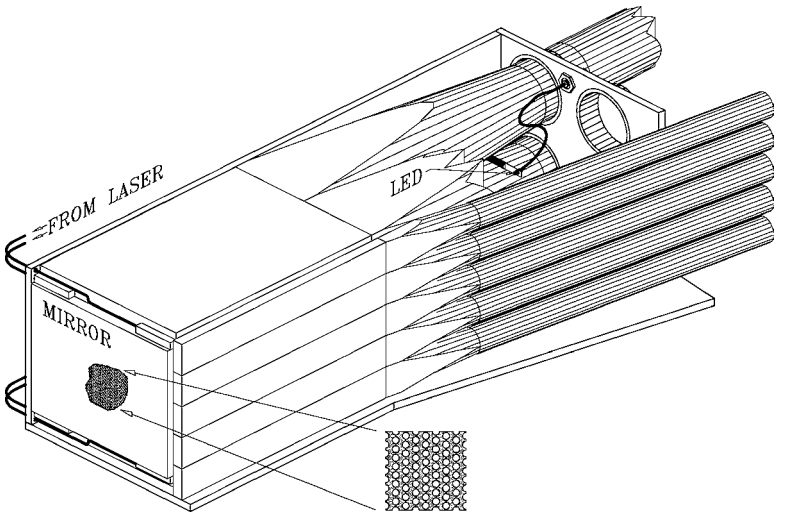

Figure 17 Schematic of a calorimeter. The detector is subdivided into four quadrants, each viewed by an independent photomultiplier tube. A pulsed nitrogen laser (337 nm) provides a time calibration pulse for selected runs. A five-finger scintillator hodoscope is shown on the front face. The inset shows the close-pack fiber-lead grid.

threshold is exceeded, a sequence of typically 32 samples (80 ns) is recorded. A representative "clean" pulse stands alone in Figure 18*a* on top of a flat pedestal within an "island" of digitizer samples. Figure 18*b* shows two pulses close in time.

5.3. Determination of ω_a

Determining ω_a from the raw data involves processing the digitized waveforms to obtain electron times and energies, building histograms of the electron time

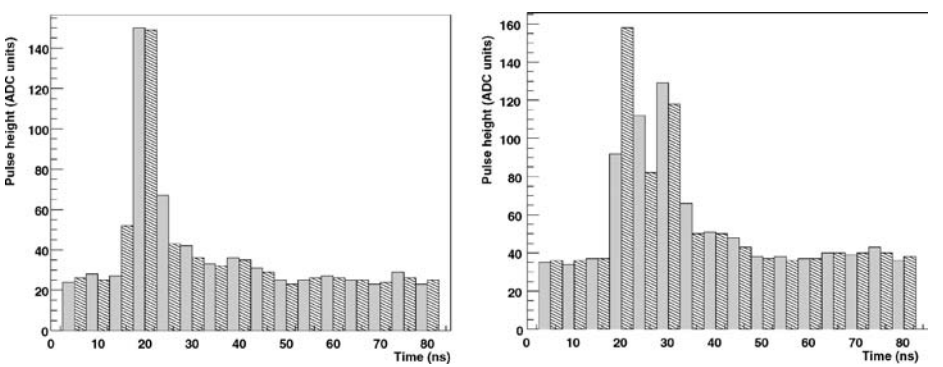

Figure 18 The left panel shows a single pulse on top of a pedestal. The right panel shows a more complicated pattern, in which two pulses appear close together in time.

spectrum, and finally developing the correct fitting function. Although the specific procedures used to analyze the data varied over the history of the experiment, the following sequence is representative of the tasks carried out to prepare the histograms for fitting:

- Raw waveform digitizer islands are scrutinized for single or multiple electron pulse candidates. A fitting procedure is used to match well-known pulse shapes with the digitized samples. Pulses separated by >3.5–5 ns (production dependent) are resolved reliably and recorded as individual events. Decay electron times and energies are listed for each detector.
- An electron energy distribution is built from a sample of late-time (pileup-free) electrons. An end-point fit establishes the absolute energy scale necessary to accurately select a common energy threshold for all detectors.
- A pileup spectrum is artificially constructed from pulses found on the recorded islands preceding and following the samples close to the trigger pulse (see Figure 18). Such pulses give an estimate of the number and energy distribution of those that remain undetected beneath the main trigger pulse. With proper bookkeeping, these pileup events can be removed, on average, from histograms built from the decay electron list. The uncorrected electron energy distribution is represented as squares in Figure 19. Artificially constructed pileup events have the energy distribution shown by triangles. The two spectra match at high energy, where only pileup events are expected.
- The pileup-corrected average electron energy is plotted versus time after injection to test the energy-scale stability. This distribution is sensitive to any

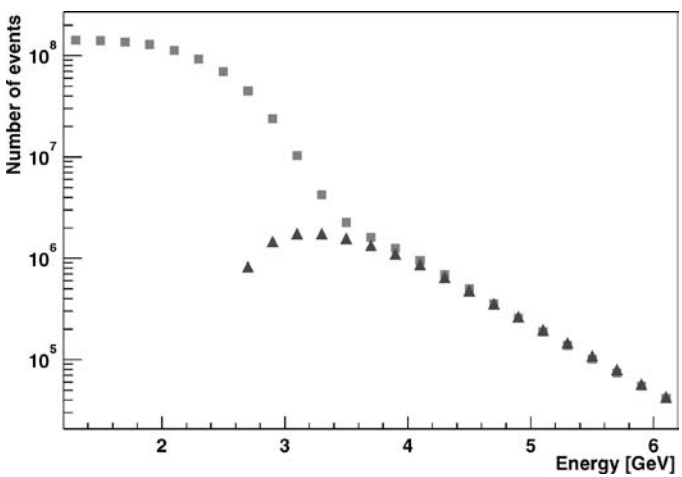

Figure 19 Energy distribution for all events (*squares*) and for pileup events (*triangles*). They match above 3.1 GeV, where all events are expected to come from multi-particle pileup.

rate-dependent gain changes in the detectors and to software energy extraction biases that depend on background or pileup (both of which change over time following injection). A function parameterizing the time dependence of the energy scale is used to correct processed pulses at the histogram-building step.

- Next, energy-scale-corrected and pileup-subtracted histograms are created for each detector and run. The injected ≈50-ns-long muon bunches expand because of the finite momentum distribution, so that after about 25 μs, when our fits start, the ring is fully populated. Histograms are built using time bins approximately equal to the cyclotron frequency (∼150 ns) and a random time in the range [−75, +75] ns is added to the start time for each muon fill. This procedure eliminates fast-rotation-dependent features. The histograms are now ready for fitting to extract ω_a.

Figure 20 shows a histogram of the four billion decay electrons from the 2000 μ^+ run. In principle, these data can be fitted to the simple five-parameter function in Equation 20. However, such a fit yields a χ^2/degree of freedom (dof) that greatly exceeds the expectation of $1 \pm \sqrt{2/\text{dof}}$. With typically 4000 dof, the requirement on the goodness of fit is ±0.02 of unity. A Fourier analysis of the residuals (see Figure 21) to the simple fit illustrates the dominant horizontal coherent betatron oscillation (CBO) frequency and its sidebands at $f_{\text{CBO}} \pm f_{g-2}$. There is no peak at the "$(g-2)$" frequency (dashed line), f_{g-2}, because the fit accounts for it. However, the peak at the beat frequency, $f_{\text{CBO}} - f_{g-2}$, is very close to the dashed line and thus potentially interferes with the proper extraction of f_{g-2} or, equivalently, ω_a.

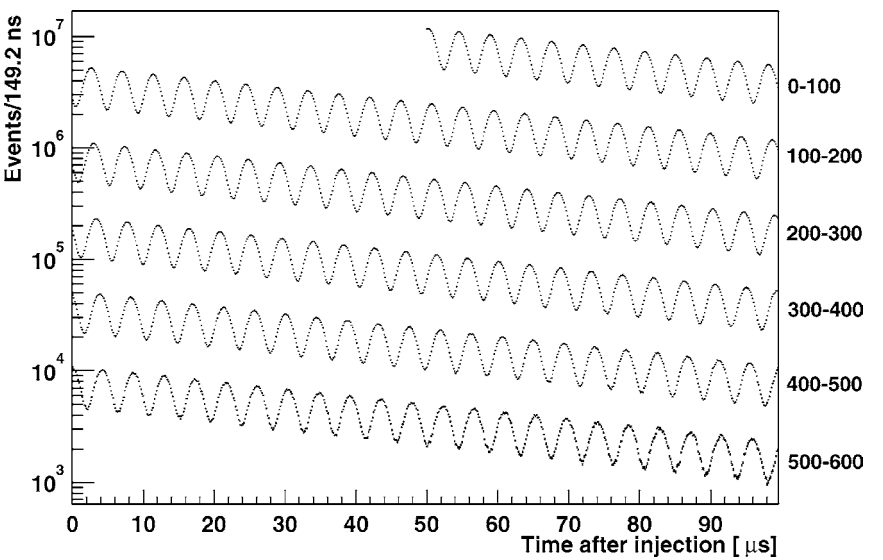

Figure 20 Distribution of counts versus time for the four billion decays in the 2000 μ^+ data taking period.

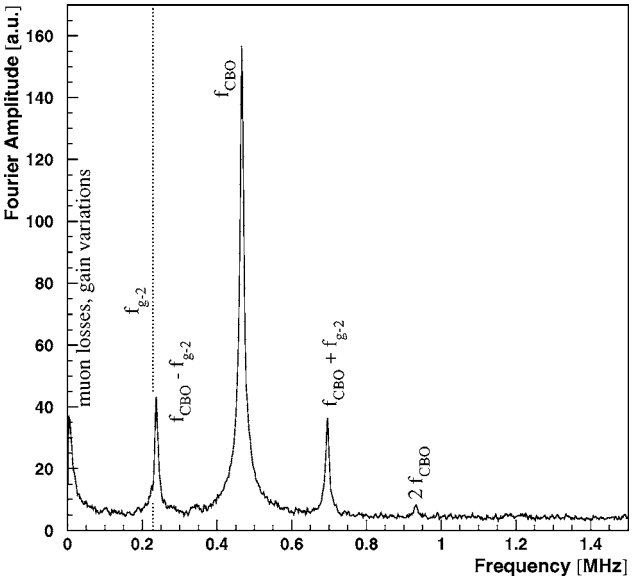

Figure 21 Fourier transform of the residuals from a fit to the 2000 data using the simple five-parameter function in Equation 20. The peaks are associated with the horizontal coherent betatron oscillation and the beat frequency with respect to f_{g-2}.

In 2001, the use of the new tune (n) values resulted in horizontal CBO frequencies that were further from twice the $(g-2)$ frequency.

The detector acceptance is a function of the muon position, the muon spin direction, and the decay electron energy. A full treatment of CBO introduces the following modifications to $N_{\rm th}$, $A_{\rm th}$, and $\phi_{\rm th}$ in Equation 20:

$$\begin{aligned} N_0 &\rightarrow N_0\left[1 + A_N e^{-t/\tau_{\rm CBO}} \cos(\omega_{\rm CBO} t + \phi_N)\right], \\ A &\rightarrow A\left[1 + A_A e^{-t/\tau_{\rm CBO}} \cos(\omega_{\rm CBO} t + \phi_A)\right], \\ \phi &\rightarrow \phi + A_\phi e^{-t/\tau_{\rm CBO}} \cos(\omega_{\rm CBO} t + \phi_\phi), \end{aligned} \qquad 22.$$

where $\tau_{\rm CBO} \simeq 100\mu$s.

Also evident in Figure 21 is a rise at low frequencies, indicating an incompletely fitted low-frequency component in the data. This is mainly due to muons that are lost from the storage ring during the fit time ($\simeq$0.5%.) A fraction of the lost muons are detected by observing the coincidence of three consecutive front hodoscope detectors.

Figure 22 shows the lost muon rate, $f_\Lambda(t)$, for the 2000 data. The effect is multiplicative on the fitting function such that

$$N(t) \rightarrow N(t) e^{-t/\gamma\tau} e^{-\int_0^t f_\Lambda(t')dt'}. \qquad 23.$$

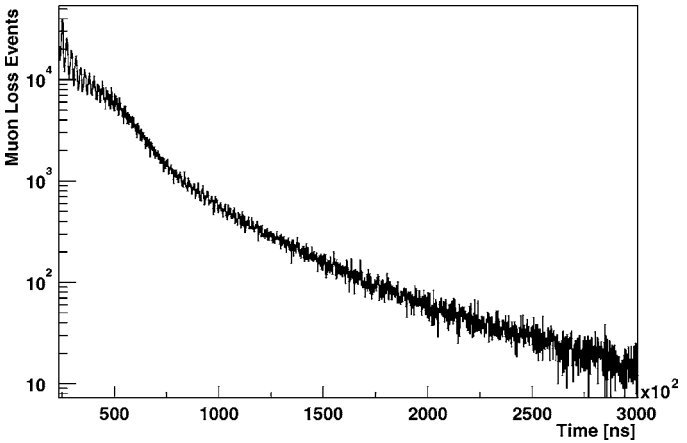

Figure 22 Muon loss events versus time after injection from the 2000 data.

The modified version of Equation 20 no longer has just five free parameters but instead includes the additional normalizations, frequencies, lifetimes, and phases associated with the known CBO and muon loss. In practice, many of these terms can be found from different studies of the data. Multiparameter fitting has been applied to all of the data summed together, to the data separated by detector, and to the data subdivided by energy. Binning the data in small energy bins optimizes the average NA^2 and reduces the statistical uncertainty. Furthermore, the data can be sorted with a weighting proportion to the energy-dependent asymmetry; this method extracts the greatest statistical power from a given data set.

As an example of the multiparameter data fitting, we choose an analysis from the 2000 μ^+ running period, in which data from nine 0.2 GeV-wide energy bins for each of the 22 detectors included were separately fitted for ω_a, the final result being an average of the 198 fits. The results illustrate consistency and stability as expected. The upper left panel of Figure 23 shows ω_a versus start time of the fit. This curve should be flat, with two thirds of its points contained within the expected bands (sideways "parabola"). The result cannot depend on either energy bin (upper right) or detector station (lower left). The normalized difference between the 198 individual fits and the average is shown in the bottom right panel. For an unbiased measurement, this distribution must be centered at zero and should have a Gaussian distribution with a width of 1.0. It does. Each of the 198 entries has statistical power equivalent to the entire CERN-III experiment!

An alternative "ratio" analysis method, which constructs a spectrum where the exponential decay and other slowly varying effects are absent, is used in addition to the multiparameter fitting. The ratio method isolates the $(g - 2)$ oscillation as the only identifiable feature in the data. Events are randomly sorted into four sets,

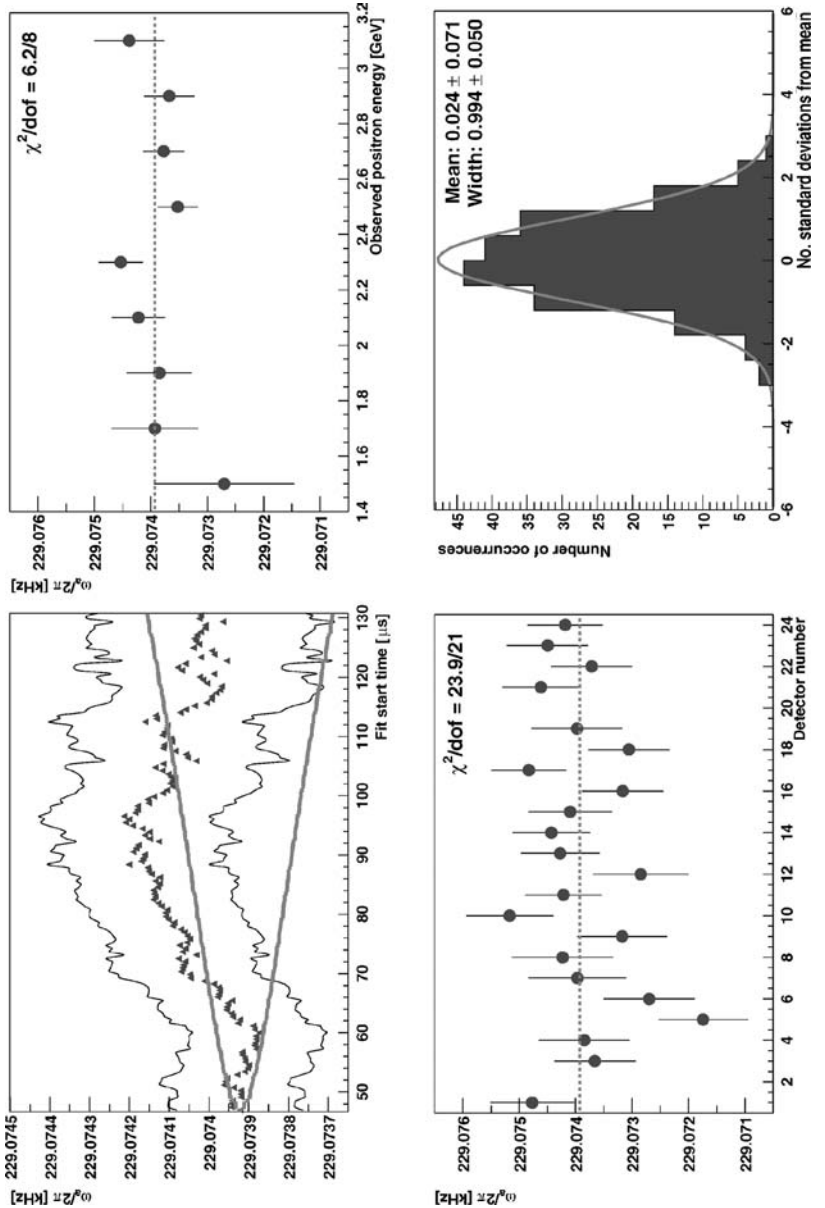

Figure 23 Fit results from an energy-binned analysis versus start time of the fit (*upper left*), energy bin (*upper right*), and detector station (*lower left*). The distribution of the 198 individual results with respect to the average is shown in the lower right panel.

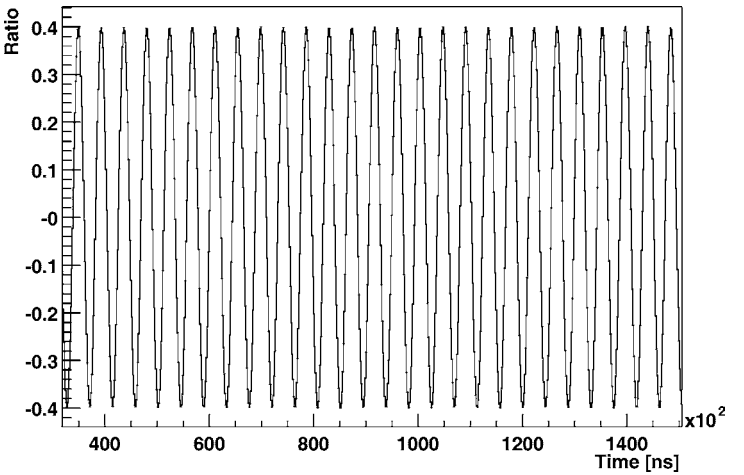

Figure 24 Data constructed by the simple "ratio method" described in the text. This histogram is from the 2001 μ^- run and includes all detectors and both tune value running periods. It was fitted, yielding an excellent χ^2/dof, to only three parameters.

A, B, C, and D. Sets A and B are time shifted by plus or minus one half of a $(g-2)$ oscillation period, respectively, and sets C and D are left unaffected. Recombined in the ratio $(A+B-C-D)/(A+B+C+D)$, this spectrum exhibits an oscillation about zero at frequency ω_a, as shown in Figure 24. It was then fitted using a three-parameter function of the form $r(t) \approx A(E)\sin[\omega_a t + \phi_a(E)]$. This simple fitting function, applied to the data summed over all detectors, gives a satisfactory fit without the need to explicitly introduce CBO terms.

5.4. Corrections to ω_a

Previously, we derived the formula for ω_a for the case of $\vec{\beta} \cdot \vec{B} = 0$ in order to illustrate the principle of the measurement. However, in our ring, the muons undergo betatron oscillations in the vertical plane, so that $\vec{\beta} \cdot \vec{B} \neq 0$. The general equation is (31)

$$\frac{d(\hat{\beta} \cdot \vec{S})}{dt} = \frac{e}{mc}\vec{S}_T \cdot \left[a\hat{\beta} \times \vec{B} + \left(\frac{g\beta}{2} - \frac{1}{\beta}\right)\vec{E}\right], \qquad 24.$$

where $\vec{S}_T$ is the component of $\vec{S}$ perpendicular to the velocity. The correction to ω_a due to vertical betatron oscillations was calculated analytically (32) and with computer tracking for each n-value setting and was typically 0.3 ppm. The horizontal betatron oscillations do not change $\vec{\beta} \cdot \vec{B}$. The term proportional to the electric field is zero only for the magic momentum. The correction to ω_a due to muons that are not at the magic momentum, also calculated analytically and with

computer tracking for each n-value setting, was typically 0.5 ppm. The input is the measured momentum distribution obtained from the fast-rotation Fourier analysis. The final correction to ω_a for the 2001 data set to account for the effects of the vertical betatron oscillations and electric field was $+(0.77 \pm 0.06)$ ppm.

5.5. Systematic Errors

A design goal of E821 was to keep the systematic uncertainties well below the statistical uncertainties. Maintaining this standard occupies the bulk of our analysis time and effort. With the data prepared and fitted to an appropriate function, obtaining a value for ω_a is relatively easy. However, it is imperative to question how well the extracted ω_a represents the true ω_a. How might the data preparation and fitting procedure influence the result? Does any term "pull" the frequency? For each of the included effects—pileup subtraction, energy-scale adjustment, CBO, muon loss—the general procedure is to explore how significantly ω_a is affected by a variance in the value of that effect. Typical of these tests are analyses performed with different pileup fractions, adjustments in the gain corrections, and variance of the parameter values for CBO and muon-loss functional modifications. In all cases, a wide range is examined and an ω_a sensitivity is established to set a systematic limit.

Table 6 lists the systematic uncertainties from the most recent μ^- analysis of ω_a. The "lost muons" entry stems mainly from the certainty with which we know that those muons that are lost carry the same phase as those that are not; we determined this sensitivity from a tracking simulation, not from a fit. The CBO systematic listed here is three times smaller than in 2000, owing to the change in n value, which moved f_{CBO} further from twice f_{g-2}.

But what happens if there is an effect that cannot be included in the preparation or fitting of the data? Then estimates must be made of the possible influence on ω_a. Here are three examples.

The AGS is loaded with 12 proton bunches in every cycle; they are extracted with 33 ms separation. Occasionally, protons can leak from the wrong bunch

TABLE 6 Systematic uncertainties for the 2001 ω_a analysis

Source of errors	**Size [ppm]**
Coherent betatron oscillations	0.07
Pileup	0.08
Gain changes	0.12
Lost muons	0.09
E-field and pitch correction	0.06
Others[a]	0.08
Total systematic error on ω_a	0.21

[a]Beam debunching, bin width, timing shifts, AGS background, fitting.

and produce a low-intensity burst that arrives at the storage ring out of time from the main bunch, but the delay is synchronized in integer multiples of the AGS cyclotron period ($\sim$2.6 μs). The particles slam into the detectors and cause spikes in the time spectrum at fixed intervals. The severity of this problem is determined by periodically taking data with the quadrupole high voltage turned off. No muons are stored, so the leakage spike time and intensity distribution are easily observed (in 2000 we installed a sweeper magnet in the beamline to block these bursts). From a measure of this background, a simulation study determined the influence on ω_a; it is small ($<$0.02 ppm after the sweeper magnet was installed).

The detector acceptance depends on the muon decay position. Changes in the muon position distribution from early to late times in the fill would change the measured value of ω_a. Analysis of the data from the scintillator counter hodoscopes in front of the calorimeters, combined with a beam-tracking calculation and a GEANT-based simulation, set a systematic error limit of 0.03 ppm on ω_a for changes in the muon vertical distribution. The muon vertical distribution could change owing to reduced voltage on the pulsed electrostatic quadrupole electrodes as a function of time after injection. Measurements of the rate of change of voltage were consistent with the design time constant of $\simeq$0.1 s.

The muon radial distribution is determined by the magnetic field strength and the momentum distribution. The magnetic field strength is stable at the 0.1 ppm level, which leads to a negligible error on ω_a. However, the momentum distribution changes from early to late times because the muon dilated lifetime is $\gamma\tau$. The average muon radius at late times is slightly larger than at early times; this, in turn, shifts the radial distribution on the calorimeter front face. The effect on ω_a—studied in a simulation, which folds in detector nonuniformity—is 0.03 ppm.

6. RESULTS AND INTERPRETATION

The results for a_μ from the five running periods are listed in Table 1. Figure 25 plots the E821 measurements. Our measured values of a_{μ^+} and a_{μ^-} are consistent, as predicted by the *CPT* theorem. The final combined experimental value is

$$a_{\mu^\pm}(\text{expt.}) = 11659208(6) \times 10^{-10} \quad [0.5\,\text{ppm}], \qquad 25.$$

where the uncertainty reflects the statistical and systematic errors combined in quadrature.

6.1. Comparison to Theory

It is remarkable that theorists can calculate the muon anomaly to an accuracy of better than one part per million. The standard-model expectation includes effects from QED, hadronic, and electroweak terms. The QED (33) and weak contributions (34) are not in doubt at the level of relevance required here. In their companion review article (35) on the muon anomalous moment theory, Davier & Marciano give, respectively,

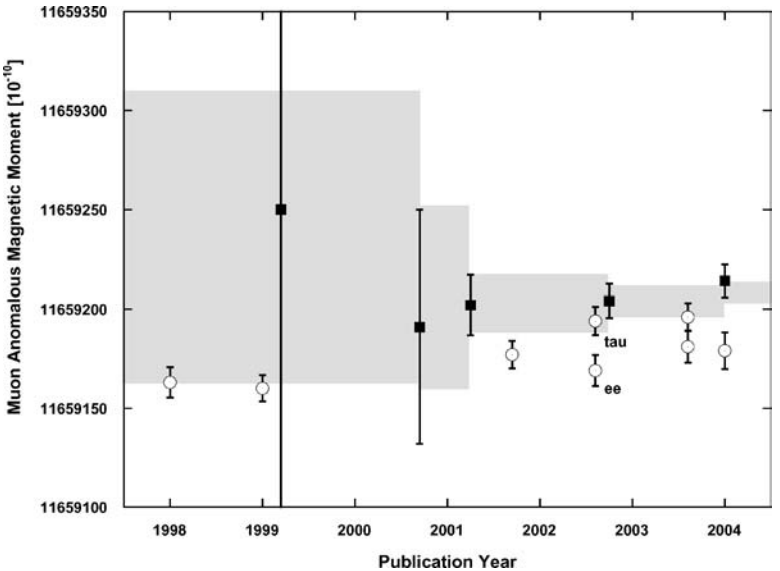

Figure 25 Results from E821 (*solid squares*) by publication year; the shaded band represents the experimental world average. Selected standard-model theory values (*open circles*) illustrate the evolution including the hadronic light-by-light sign change in 2001 and the current distinction between e^+e^--based and tau-based evaluations of the hadronic vacuum polarization.

$$a_\mu(\text{QED}) = 11658472.07(0.11) \times 10^{-10} \quad (0.01\,\text{ppm}) \qquad 26.$$

and

$$a_\mu(\text{weak}) = 15.4(0.2) \times 10^{-10} \quad (0.02\,\text{ppm}). \qquad 27.$$

The lowest-order hadronic vacuum polarization (HVP) contribution cannot be calculated with good accuracy from first principles; however, the cross section $e^+e^- \rightarrow$ hadrons can be combined with a dispersion relation to determine the HVP contribution. Indirectly, tau-decay data can also be used if the conserved vector current hypothesis is assumed and appropriate isospin corrections are applied. However, the e^+e^- and tau data are incompatible (see (35)), which leads to the usual practice of quoting distinct evaluations of a_μ(HVP) using each approach.

A third technique to determine HVP has recently been developed. An initial-state emitted photon in the radiative-return method lowers the effective center-of-mass energy of an e^+e^- collision. This allows $e^+e^- \rightarrow$ hadrons data to be obtained across a broad $\sqrt{s}$ range up to the fixed collision energy of the collider, which is usually centered on a vector resonance such as the ϕ or Υ meson. The KLOE Collaboration (36) reports a new measurement of the important

$e^+e^- \to \pi^+\pi^-$ cross section in an energy region that brackets the ρ-resonance. The KLOE data support the CMD-II e^+e^- scan performed at Novosibirsk (37) and, importantly, are also in conflict with the tau-decay data. The KLOE result is the first independent evidence supporting the direct e^+e^- approach to determine the HVP.

Higher-order hadronic processes are also significant. Whereas the three-loop contribution can be estimated reliably based on data, the hadronic light-by-light (HLbL) evaluation is model-dependent and less certain. Theoretical developments by Melnikov & Vainshtein (38), coupled with additional adjustments introduced by Davier & Marciano, lead to the new estimate

$$a_\mu(\text{HLbL}) = 12.0(3.5) \times 10^{-10} \quad (0.3\,\text{ppm}). \qquad 28.$$

Summarizing, the e^+e^--based standard-model (SM) evaluation is (35, 39, 40)

$$a_\mu(\text{SM}, e^+e^-\text{-based}) = 11659184(8) \times 10^{-10} \quad (0.69\,\text{ppm}), \qquad 29.$$

and the tau-based approach yields

$$a_\mu(\text{SM, tau-based}) = 11659200(7) \times 10^{-10} \quad (0.60\,\text{ppm}). \qquad 30.$$

Figure 25 shows the measured and (representative) calculated values of the muon anomaly for the period 1998–2004. The final experimental result is larger than theory by either $2.4\,\sigma$ (e^+e^-) or $0.9\,\sigma$ (tau). A difference has persisted between experiment and theory over the duration of the experiment. The difference has prompted a considerable theoretical dialogue related to standard-model extensions as well as refinements to the basic theory. Additional e^+e^- data from CMD-2 (37), KLOE (36), and the *B*-factory experiments (41) will help to reduce the theoretical uncertainty. Meanwhile, our E821 Collaboration is designing an upgrade aimed at reducing the experimental measurement uncertainty to a level of 0.20 ppm. If a significant difference between theory and experiment exists after these improvements are made, the message will be clear: It's time to rewrite the standard model.

ACKNOWLEDGMENTS

We offer our deepest thanks to our colleagues in the E821 Collaboration and to our theoretical colleagues who have worked on computing a_μ contributions. We have been deeply enriched by sharing in the effort, led by Vernon W. Hughes, to perform a beautiful experiment and possibly to discover something new about physics. The $(g-2)$ experiment is supported in part by the U.S. Department of Energy, the U.S. National Science Foundation, the German Bundesminister für Bildung und Forschung, the Russian Ministry of Science, and the U.S.-Japan Agreement in High Energy Physics.

The *Annual Review of Nuclear and Particle Science* is online at http://nucl.annualreviews.org

LITERATURE CITED

1. Feynman R. *Elementary Particles and the Laws of Physics, The 1986 Dirac Memorial Lectures*, pp. 1–60. Cambridge, UK: Cambridge Univ. Press (1987)
2. Dirac PAM. *Theory of electrons and positrons.* http://www.nobel.se/physics/laureates/1933/dirac-lecture.pdf (1933)
3. Close FE. *An Introduction to Quarks and Partons*, pp. 62–64. New York: Academic (1979)
4. Waller I. *The 1965 Nobel Prize in Physics.* http://www.nobel.se/physics/laureates/1965/press.html (1965)
5. Waller I. *The 1955 Nobel Prize in Physics.* http://www.nobel.se/physics/laureates/1955/press.html (1955)
6. Yukawa H. *Meson theory in its developments.* http://www.nobel.se/physics/laureates/1949/yukawa-lecture.pdf (1949)
7. Hagiwara K, et al. (Particle Data Group). *Phys. Rev. D* 66:010001 (2002) http://www.aps.org/units/dpf/quarks_unbound/ (2002)
8. Nagel B. *The 1979 Nobel Prize in Physics.* http://www.nobel.se/physics/laureates/1979/presentation-speech.html (1965)
9. Hughes VW, Kinoshita T. *Comments Nucl. Part. Phys.* 14:341 (1985)
10. Nilles H. *Phys. Rep.* 110:1 (1984); Haber H, Kane G. *Phys. Rep.* 117:75 (1985)
11. Lopez JL, Nanopoulos DV, Wang X. *Phys. Rev. D* 49:366 (1994)
12. Klein OB. *The 1957 Nobel Prize in Physics.* http://www.nobel.se/physics/laureates/1957/press.html (1957)
13. Hughes VW. *Annu. Rev. Nucl. Part. Sci.* 50:i (2000)
14. Charpak G, et al. *Nuovo Cim. Soc. Ital. Fis.* 37:1241 (1965)
15. Bailey J, et al. *Nuovo Cim. Soc. Ital. Fis. A* 9:369 (1972)
16. Bailey J, et al. *Nucl. Phys. B* 150:1 (1979)
17. Bargmann V, Michel L, Telegdi V. *Phys. Rev. Lett.* 2:435 (1959)
18. Liu W, et al. *Phys. Rev. Lett.* 82:711 (1999)
19. Carey RM, et al. ($g-2$ Collab.) *Phys. Rev. Lett.* 82:1132 (1999)
20. Brown HN, et al. ($g-2$ Collab.) *Phys. Rev. D* 62:091101 (2000)
21. Brown HN, et al. ($g-2$ Collab.) *Phys. Rev. Lett.* 86:2227 (2001)
22. Bennett GW, et al. ($g-2$ Collab.) *Phys. Rev. Lett.* 89:101804 (2002)
23. Bennett GW, et al. ($g-2$ Collab.) *Phys. Rev. Lett.* 92:161802 (2004)
24. Yamamoto A, et al. *Nucl. Instrum. Methods A* 491:23 (2002)
25. Danby GT, et al. *Nucl. Instrum. Methods A* 457:151 (2001)
26. Efstathiadis E, et al. *Nucl. Instrum. Methods A* 496:8 (2003)
27. Semertzidis Y, et al. *Nucl. Instrum. Methods A* 503:458 (2003)
28. Prigl R, et al. *Nucl. Instrum. Methods A* 374:118 (1996)
29. Fei X, Hughes VW, Prigl R. *Nucl. Instrum. Methods A* 394:349 (1997)
30. Sedykh SA, et al. *Nucl. Instrum. Methods A* 455:346 (2000)
31. Jackson JD. *Classical Electrodynamics*, pp. 556–60. New York: Wiley (1975)
32. Farley FJM, Picasso E. *Quantum Electrodynamics*, pp. 479–559. Singapore: World Sci. (1990)
33. Mohr P, Taylor B. *Rev. Mod. Phys.* 72:351 (2000)
34. Czarnecki A, Marciano WJ. *Phys. Rev. D* 64:013014 (2001)
35. Davier M, Marciano WJ. *Annu. Rev. Nucl. Part. Sci.* 54:115–40 (2004)

36. Denig A, et al. (KLOE Collab.) hep-ex/0311012 (2003)
37. Akhmetshin RR, et al. (CMD-2 Collab.) *Phys. Lett.* B578:285 (2004)
38. Melnikov K, Vainshtein A. hep-ph/0312226
39. Davier M, Eidelman S, Höcker A, Zhang Z. *Eur. Phys. J. C* 31:503 (2003)
40. Ghozzi S, Jegerlehner F. *Phys. Lett.* B583: 222 (2004)
41. Davier M. (BaBar Collab.) hep-ex/0312063 (2003)

Figure 4 Completed muon storage ring. Photo courtesy of R. Bowman.

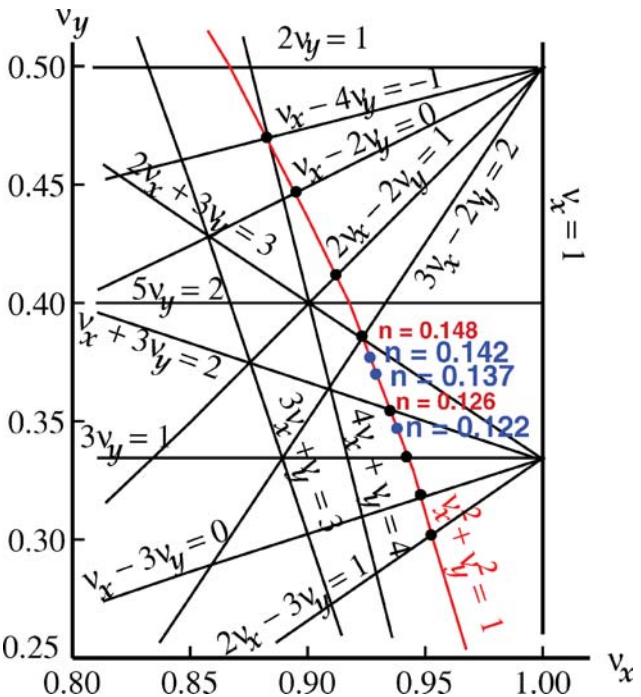

Figure 7 The vertical tune versus the horizontal tune showing the working line and resonance lines up to fifth order.

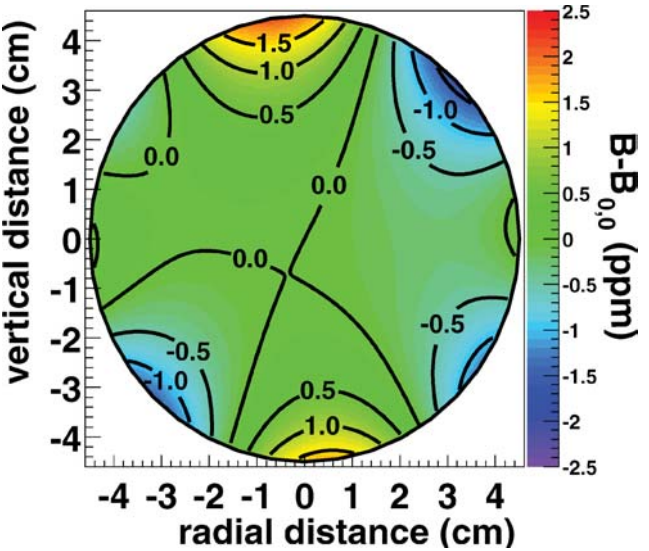

Figure 12 A two-dimensional multipole expansion of the B field during the 2001 run, averaged over azimuth from one out of 20 trolley measurements. Half ppm contours with respect to a central azimuthal average field $B_0 = 1.451\,269$ T (2001 data) are shown.